NUMERICAL ANALYSIS AND DESIGN OF COLD-FORMED HIGH STRENGTH STEEL RHS X-JOINTS AT ELEVATED TEMPERATURES

Madhup Pandey*,[1] and Ben Young[2]

[1]*Department of Civil Engineering, University of Nottingham, Nottingham, United Kingdom*
[2]*Department of Civil and Environmental Engineering, The Hong Kong Polytechnic University, Hong Kong, China*

Abstract

A numerical program is carried out in this study with an aim to investigate the static performance of cold-formed high strength steel (CFHSS) X-joints with square and rectangular hollow section (SHS and RHS) braces and chords at elevated temperatures. The numerical investigation was performed through the finite element (FE) method using mechanical properties at elevated temperatures. The FE models developed and validated by the authors for identical CFHSS X-joints at room temperature and post-fire conditions were used in this study to perform numerical investigation at elevated temperatures. The SHS and RHS X-joints were subjected to axial compression loads through brace members. The validated FE models were used to perform a comprehensive FE parametric study at 400°C, 500°C, 600°C and 1000°C that comprised in total 756 FE specimens. Using mechanical properties at elevated temperatures, nominal resistances were predicted from design rules given in European code and *Comité International pour le Développement et l´Etude de la Construction Tubulaire* (CIDECT) and compared with the residual strengths of the investigated X-joints. Overall, SHS and RHS X-joint specimens were failed by chord face failure, chord side wall failure and a combination of these two failure modes. Generally, predictions from design rules given in European code and CIDECT are quite conservative but scattered and unreliable. Therefore, economical and reliable design equations are proposed in this study for predicting the resistances of cold-formed steel RHS X-joints made of S900 steel grade at elevated temperatures.

Keywords: Cold-formed steel; Design equations; Elevated temperature; FE analysis; High strength steel; X-joints.

*Corresponding author. (e-mail: madhup.pandey@nottingham.ac.uk).

1. Introduction

Welded tubular joints are integral parts of tubular structures which can be frequently seen in various onshore and offshore structures. In order to ensure the integrity of the overall structure, adequate performance of joints under different adverse conditions is a prerequisite. Owing to the presence of geometric discontinuity, stress concentration, complex failures, residual stresses and fabrication defects, tubular joints need more careful design considerations over tubular members. It is widely known that the mechanical properties of steel are very sensitive to elevated temperatures (T). Due to considerable degradation of strength and stiffness of steel material at high elevated temperatures, a tubular joint could fail at a load significantly smaller than its joint resistance at room temperature. This could result in a progressive or sudden collapse of the entire structure. Thus, an investigation looking into the structural performance of tubular joints at elevated temperatures needs urgent attention. High strength steel (HSS) (i.e. steel grade higher than S460) hollow section members are in high demand in various civil engineering projects because of their superior strength per unit weight, improved toughness and reduced handling costs. The production of HSS hollow section members has ramped up in the last decade due to substantial growth in the steel and manufacturing sectors. However, the lack of adequate research work and design recommendations are the primary reasons hampering the widespread use of high strength structural steels. The authors have conducted a series of experimental investigations [1-5] on HSS rectangular hollow section (RHS) T- and X-joints. In addition, Pandey et al. [6,7] proposed design rules for predicting the static strengths of cold-formed S900 and S960 steel grades RHS T- and TF-joints. Moreover, Lan et al. [8,9] carried out experimental and numerical investigations on box-section T- and X-joints with steel grades ranging from S460 to S960.

It should be noted that the aforementioned investigations [1-9] were carried out to investigate the static behaviour of HSS T- and X-joints at room temperature. To the best of the authors' knowledge, currently, no investigation is available on the static performance of any type of HSS tubular joint at elevated temperatures. Although some investigations have been carried out in the past two decades on the static behaviour of various types of uniplanar and multiplanar hollow section joints at elevated temperatures, however, all these studies were conducted on normal strength steel (i.e. steel grade less than and equal to S460) joints with a primary focus on circular hollow section (CHS) joints. A brief review of previous studies on the structural performance of different types of tubular joints at elevated temperatures is presented in Section 2 of this paper.

An extensive numerical investigation was performed in this study to investigate the elevated temperature joint resistances ($N_{f,T}$) of cold-formed high strength steel (CFHSS) square hollow section (SHS) and RHS X-joints. In this paper, from this point forward, RHS will include SHS. In this study, the static performance of CFHSS RHS X-joints undergoing compression loads was numerically studied at four elevated temperatures, including 400°C, 500°C, 600°C and 1000°C. Currently, none of the international codes and guides includes design rules to predict the resistances of tubular joints at elevated temperatures. Therefore, in this study, design equations proposed by Pandey and Young [10] for CFHSS RHS X-joints at room temperature were modified to propose accurate and reliable design rules for cold-formed steel RHS X-joints made of S900 steel grade at elevated temperatures. In addition, the appropriateness of current design rules given in EC3 [11] and CIDECT [12], using mechanical properties at elevated temperatures, was also evaluated for the investigated X-joints.

2. Review of investigations conducted on tubular joints subjected to elevated temperatures

Lan and Huang [13] numerically investigated the joint resistances of duplex, austenitic and AISI 304 stainless steel RHS T- and X-joints at elevated temperatures and proposed design equations for their ultimate resistances. Lan et al. [14] numerically studied the static performance of duplex, austenitic and AISI 304 stainless steel RHS K- and N-joints at elevated temperatures. In addition, design rules were also proposed in Ref. [14] using residual yield strengths. Feng and Young [15] carried out a numerical investigation on duplex and AISI 304 stainless steel RHS T- and X-joints using mechanical properties at elevated temperatures proposed by Chen and Young [16]. Design rules were proposed by applying temperature correction factors on design equations given in CIDECT [12]. Nassiraei et al. [17] proposed design equations for CHS X-joints at elevated temperatures, where specimens were reinforced with collar plates. Two methods for predicting the ultimate capacities of CHS T-joints at elevated temperatures were proposed by Shao et al. [18] that duly investigated the effects of critical geometric parameters. Using non-linear regression analysis, Dodaran et al. [19] proposed a design formula to predict the resistance of KT-joints at elevated temperatures. Chen et al. [20] studied the static performance of CHS T-joints with ring stiffeners at elevated temperatures and finally proposed design equations for predicting the residual resistances of the investigated joints. Using transient state analysis, Gao et al. [21] studied the structural behaviour of CHS T-joints with collar plates. The residual resistances of concrete-filled CHS T-joints after fire exposures were studied by Gao et al. [22]. The influence of critical geometric parameters on the residual resistances of CHS T-joints at elevated temperatures was studied by Cheng et al. [23].

Static performance of CHS T-joint without internal stiffeners was studied by Tan et al. [24] using experimental and numerical methods. It was reported that the joint resistance sharply reduced at high temperatures. The residual joint resistances of CHS T-joints subjected to brace in-plane bending load were investigated by Fung et al. [25] at elevated temperatures. Ozyurt et al. [26] numerically investigated the joint resistances of CHS and SHS T-, Y-, X-, K- and N-joints at elevated temperatures. Based on numerical results, reduction factors were then proposed to estimate the residual resistances of the investigated joints. Ozyurt et al. [27] numerically investigated the joint resistances of elliptical hollow section (EHS) T- and X-joints at elevated temperatures. The critical temperature of CHS K-joints was determined using the deformation rate based criterion in He et al. [28]. Full-scale CHS T-joints subjected to compression loads were experimentally and numerically studied at elevated temperatures by Nguyen et al. [29,30]. The residual resistances of impacted CHS T-joints at elevated temperatures were investigated by Yu et al. [31]. The post-fire residual capacities of CHS T-joints were experimentally studied by Jin et al. [32]. Liu et al. [33] performed a numerical parametric study to investigate the static behaviour of CHS T-joints at elevated temperatures. The structural performance of CHS T-joints subjected to blast and fire was experimentally studied by Yu et al. [34]. The technique of artificial neural network was used by Xu et al. [35] to estimate the resistances of CHS T-joints at elevated temperatures.

3. Methodology

This section summarises the overall methodology used in the numerical investigation presented in this paper. The numerical investigation was conducted using ABAQUS [36]. The static resistances of CFHSS RHS X-joints subjected to compression loads were numerically investigated at 400°C, 500°C, 600°C and 1000°C. In the absence of any experimental investigation on CFHSS RHS X-joints at elevated temperatures, the numerical investigation in this study was performed using the finite element (FE) models developed and validated by Pandey and Young [10] for cold-formed S900 and S960 steel grades X-joints at room temperature. It is important to note that similar FE models were successfully used by Pandey and Young [37] to validate the test results of fire exposed (i.e. post-fire) cold-formed S900 and S960 steel grades X-joints using post-fire mechanical properties. As natural fires have different temperature vs time curves and also due to substantial cost involved in a fire test, numerical studies are popularly used for such investigations. It is due to these reasons, the FE models of tubular joints validated against room temperature test results were used in many numerical studies [13-15,26,27,38-50] for their corresponding elevated temperatures investigations.

The numerical investigation in this study was performed using the constitutive stress-strain model proposed by Li and Young [51] for S900 steel grade tubular members at elevated temperatures. The tubular members used in Pandey and Young [10,37] and Li and Young [51,52] were produced by the identical manufacturer with similar chemical compositions, therefore, the constitutive stress-strain model proposed by Li and Young [51] at elevated temperatures can safely be used in this study. Li and Young [52] carried out a test program to investigate the material properties of cold-formed high strength steel at elevated temperatures. The coupon specimens were extracted from the flat regions of cold-formed high strength steel RHS with nominal yield stresses of 700 and 900 MPa at ambient temperature. The coupon tests were conducted by both steady and transient state test methods for temperatures up to 1000°C. Material properties including thermal elongation, elastic modulus, yield stress, ultimate strength, ultimate strain and fracture strain were obtained from the tests. The test results were compared with the design values obtained from the European, American, Australian and British standards. The comparison results revealed the necessity of proposing specified design rules for material properties of cold-formed high strength steel at elevated temperatures. As a result, new design curves to determine the deterioration of material properties of high strength steel at elevated temperatures have been proposed. The design curves proposed by Li and Young [52] are suitable for both cold-formed and hot-rolled high strength steel materials with nominal yield stresses ranged from 690 to 960 MPa at ambient temperature. The numerical investigation was then performed using the mechanical properties predicted from the stress-strain model [51] at 400°C, 500°C, 600°C and 1000°C. The stress-strain curves of cold-formed S900 steel grade tubular member obtained from steady state tests for temperatures ranging from 100°C to 1000°C are reported in Li and Young [52]. It should be noted that for temperatures less than 400°C, the deterioration of mechanical properties of cold-formed S900 steel grade tubular member was insignificant. As reported by Li and Young [52], the residual values of ultimate strength of cold-formed S900 steel grade tubular member at 400°C, 500°C, 600°C and 1000°C were 83%, 60%, 35% and 2% of the corresponding ultimate strength at room temperature. Therefore, in order to investigate a wide range of strength reductions at elevated temperatures, the numerical investigation in this study was performed at 400°C, 500°C, 600°C and 1000°C.

4. Summary of experimental investigations conducted on cold-formed high strength steel RHS X-joints at room temperature and post-fire conditions

At room temperature, the static performance of cold-formed S900 and S960 steel grades RHS X-joints was experimentally investigated by Pandey and Young [3]. The braces and chords were welded using robotic metal active gas welding. In total, 34 tests were conducted, where test specimens were axially compressed via braces. The nominal 0.2% proof stresses of tubular members were 900 and 960 MPa. In the experimental investigation [3], β (b_1/b_0) varied from 0.34 to 1.0, τ (t_1/t_0) varied from 0.53 to 1.28, 2γ (b_0/t_0) varied from 20.2 to 38.9 and h_0/t_0 varied from 12.7 to 39.0. The symbols b, h, t and R stand for cross-section width, depth, thickness and external corner radius of RHS member, respectively. The subscripts of the symbols 0 and 1 denote chord and brace, respectively. Fig. 1 presents various notations for RHS X-joints. The failure modes identified in the tests were chord face failure (F), chord side wall failure (S) and a combination of these two failure modes, named combined failure (F+S). The lengths of braces (L_1) were equal to two times the maximum of brace cross-section width (b_1) and depth (h_1). On the other hand, the lengths of chords (L_0) were equal to $h_1 + 4h_0$ [3]. The test results were obtained in the form of N vs u and N vs v curves, where N, u and v stand for static load, chord face indentation and chord side wall deformation, respectively.

The static behaviour of cold-formed S900 and S960 steel grades fire exposed RHS X-joints was investigated by Pandey and Young [53]. Before conducting the static joint tests, the test specimens were subjected to a total of three fire exposures with preselected post-fire peak temperatures (ψ) equal to 300°C, 550°C and 750°C, respectively. In total, 16 tubular X-joints were tested under compression. The nominal 0.2% proof stresses of without fire exposed tubular members were 900 and 960 MPa. The braces and chords were welded using robotic metal active gas welding. The test specimens were exposed to fire inside a gas furnace, where the furnace temperature was increased in accordance with the ISO-834 [54]. After attaining the preselected post-fire peak temperatures (ψ), the test specimens were allowed to naturally cool inside the furnace. Subsequently, at room temperature, RHS X-joint test specimens were axially compressed through brace members. In the test program [53], β varied from 0.41 to 1.0, τ varied from 0.77 to 1.01, 2γ varied from 25.1 to 35.2 and h_0/t_0 varied from 15.2 to 35.6.

5. Details of numerical investigations conducted on cold-formed high strength steel RHS X-joints at room temperature and post-fire conditions

5.1. General

The numerical investigations on cold-formed S900 and S960 steel grades RHS X-joints at room temperature and post-fire conditions were conducted using ABAQUS [36]. The static (general) analysis procedure given in ABAQUS [36] was used as the solver. As the induced strains in the FE model during the applied load were unidirectional (i.e. no load reversal), the isotropic strain hardening law was selected for the analysis. The von-Mises yield criterion is generally the default criterion used to predict the onset of yielding in most metals, except for porous metals. Therefore, the yielding onsets of FE models in this study were based on the von-Mises yield theory. In the FE analyses, the growth of the time step was kept non-linear in order to reduce the overall computation time. Furthermore, the default Newton-Raphson method was used to find the roots of non-linear equilibrium equations. In addition to the accuracy associated with the Newton-Raphson method, one of the other benefits of using this numerical technique is its quadratic convergent approach, which in turn significantly increases the convergence rate of non-linear problems.

The material non-linearities were considered in the FE models developed for room temperature and post-fire conditions by assigning the measured values of room temperature and post-fire static stress-strain values of flat and corner portions of RHS members. However, experimentally obtained constitutive material curves both at room temperature and post-fire conditions were transformed into true stress-strain curves prior to their inclusion in the FE models. On the other hand, the geometric non-linearities in both room temperature and post-fire FE models were considered by enabling the non-linear geometry parameter (*NLGEOM) in ABAQUS [36], which allowed FE models to undergo large displacement during the analyses. Furthermore, various parameters, including through-thickness division, contact interactions, mesh seed spacing, corner region extension and element types, were also studied and reported in the following sub-sections of this paper. The labelling of both room temperature and post-fire FE specimens was kept identical to the label system used in their corresponding test programs [3,53]. Fig. 2 presents typical FE RHS X-joint specimens modelled for room temperature and post-fire numerical investigations [10,37].

5.2. Element type, mesh spacing and mechanical properties

Except for the welds, all other parts of both room temperature and post-fire FE models were developed using second-order hexahedral elements, particularly using the C3D20 elements. On the other hand, the second-order tetrahedral element, C3D10, was used to model the weld parts due to their complicated shapes. The weld parts were freely meshed using the free-mesh algorithm, however, brace and chord parts were meshed using the structure-mesh algorithm. The use of solid elements helped in making realistic fusions between tubular and weld parts of FE models. Convergence studies were conducted using different mesh sizes, and finally, chord and brace members were seeded at 4 mm and 7 mm intervals, respectively, along their corresponding longitudinal and transverse directions. Moreover, the seeding spacings of weld parts reciprocated the seeding spacings of their respective brace parts. In order to assure the smooth transfer of stresses from flange to web regions, the corner portions of RHS were split into ten elements. FE analyses were also conducted to examine the influence of divisions along the wall thickness (t) of RHS members. The results of these FE analyses demonstrated the trivial influence of wall thickness divisions on the load vs deformation curves of the investigated RHS X-joints. The use of the C3D20 element as well as the small thickness of test specimens [3,53] lead to such observations. It is worth noting that similar findings were also obtained in other studies [6,7,55]. Thus, for the validations of both room temperature and post-fire FE models, the wall thickness of tubular members was not divided. The measured values of room temperature and post-fire static stress-strain curves of flat and corner portions of RHS members [1,56] were used in the corresponding FE models. In addition, the influence of cold-working was included in the FE models by assigning wider corner regions. Various distances for corner extension were considered in the sensitivity analyses, and finally, the corner portions were extended by $2t$ into the neighbouring flat portions, which was in agreement with other studies conducted on CFHSS tubular members and joints [6,7,57-59].

5.3. Weld modelling and contact interactions

The welds were modelled in both room temperature and post-fire FE models using the average values of measured weld sizes reported in test programs [3,53]. The fillet weld was modelled for FE specimens when $\beta \leq 0.80$. However, when $\beta > 0.80$, fillet and groove welds (FW and GW) were modelled along the chord face and chord side directions, respectively. The inclusions of weld geometries appreciably improved the overall accuracies of FE models. In addition, modelling of weld parts helped attain realistic load transfer between brace and chord members, which facilitated in obtaining the actual joint behaviour. The selection of the C3D10 element maintained optimum stiffness around the joint perimeter due to its ability of taking complicated shapes. A contact interaction was defined between brace and chord members of the FE models. In addition, a tie constraint was also established between the weld and tubular members of the FE models. The contact interaction was established using the built-in surface-to-surface contact definition. The contact interaction between brace and chord members of FE models was kept frictionless. Along the normal direction of the contact interaction, a 'hard' contact pressure overclosure was used. In addition, finite sliding was permitted between the interaction surfaces. For both contact interaction and tie constraint, the surfaces were connected to each other using the 'master-slave' algorithm technique. This technique permits the separation of fused surfaces under tension, however, it does not allow penetration of fused surfaces under compression. For the brace-chord interaction, the cross-section surfaces of the braces connected to the chord member were assigned as the 'master' regions (relatively less deformable), while the chord connecting surfaces were assigned as the 'slave' regions (relatively more deformable). For the weld-tubular member tie connection, the weld surfaces were assigned as the 'master' regions, while the connecting brace and chord surfaces were assigned as the 'slave' regions.

5.4. Boundary conditions and load application

In order to assign boundary conditions in both room temperature and post-fire FE models, two reference points were created in each RHS X-joint FE specimen. The top and bottom reference points (TRP and BRP) were created at the cross-section centre of braces, as shown in Fig. 2. Subsequently, TRP and BRP were coupled to their respective brace end cross-section surfaces using the kinematic coupling type. In order to exactly replicate the test setup, all degrees of freedom (DOF) of TRP were restrained. On the other hand, except for translation along the height of the FE specimen, all other DOF of BRP were also restrained. Moreover, all DOF of other nodes of FE specimen were kept unrestrained for rotation and translation. Using the displacement control method, compression load was then applied at the BRP of FE models. In addition, the size of the step increment was kept small in order to obtain the smooth load vs deformation curves. Consequently, the boundary conditions and load application in FE analyses were identical to those used in the test programs [3,53].

5.5. Geometric imperfection in chord webs

Garifullin et al. [60] studied the influence of geometric imperfections on the behaviour of cold-formed steel hollow section joints. The imperfection profiles of RHS joints were obtained by performing elastic buckling analyses in ABAQUS [36]. The first mode of elastic buckling analysis of the FE specimen was treated as the imperfection mode of that specimen. The deformation scale of the first buckling mode was then ramped up to match the tolerance limits given in EN [61]. The scaled eigenmode shape was then superimposed on the FE model by Garifullin et al. [60]. It was concluded that geometric imperfections had a trivial influence on the static behaviour of hollow section joints. However, Pandey et al. [6] reported that the maximum measured values of cross-section width and depth of RHS members were on an average 2.9% more than their respective nominal dimensions. As tubular members used in the room temperature and post-fire experimental investigations of RHS X-joints [3,53] also belonged to the identical batch of tubes used in Refs. [1,6], therefore, it was necessary to model this geometric imperfection as an outward bulging 3-point convex arc, as shown in Fig. 3. Also, as all failure modes in test [1] and numerical investigation [6] were only governed by the deformation of chord members, therefore, Pandey et al. [6] numerically examined the influence of outward bulging of chord cross-section on the static behaviour of RHS joints. Finally, it was concluded that the effect of convex bulging of chord cross-section was only significant for equal-width (i.e. β=1.0) RHS joints [6]. As a result, in both room temperature and post-fire FE models [10,37], geometric imperfections were introduced as a 3-point convex arc in the chord webs of equal-width RHS X-joints using the measured values of maximum chord cross-section widths (b_0) of such X-joints.

5.6. Validations of room temperature and post-fire RHS X-joint FE models

Both room temperature and post-fire FE models of cold-formed S960 steel grade RHS X-joints [10,37] were developed using the modelling techniques described in the preceding sub-sections of this paper. The validations of FE models were confirmed by duly comparing the joint resistances, load vs deformation curves and failure modes between tests [3,53] and corresponding FE [10,37] specimens. The measured dimensions of tubular members and welds were used to develop all FE models. In addition, measured room temperature and post-fire static mechanical properties of flat and corner portions of cold-formed S960 steel grade tubular members were used in the validations of corresponding room temperature and post-fire FE models. It is worth mentioning that for both room temperature and post-fire investigations, the peak load or 3% deformation limit load, whichever occurred earlier in the N vs u curve, was taken as the joint resistance [12]. For the room temperature investigation on cold-formed S960 steel grade RHS X-joints, the overall values of the mean (P_m) and coefficients of variation (COV) (V_p) of the comparisons between test and FE resistances were 1.01 and 0.016, respectively [10]. Besides, on using the similar FE models with post-fire static mechanical properties, the overall values of P_m and V_p of comparisons between post-fire test and FE resistances were 1.00 and 0.006, respectively [37]. In addition, the comparisons of load vs deformation curves between test and FE RHS X-joint specimens for room temperature and post-fire investigations are shown in Figs. 4 and 5, respectively. Furthermore, Figs. 6 and 7 present comparisons of distinct failure modes between typical test and FE RHS X-joint specimens for room temperature and post-fire investigations, respectively. Hence, it can be concluded that the verified FE models precisely replicated the overall static behaviour of cold-formed S960 steel grade RHS X-joints for both room temperature and post-fire investigations [10,37].

6. Numerical investigation conducted on cold-formed high strength steel RHS X-joints at elevated temperatures

6.1. Parametric study

The FE models developed and validated by the authors for both room temperature and post-fire investigations of cold-formed S960 steel grade RHS X-joints [10,37] were used to perform parametric study in this investigation. In the parametric study, the static performance of RHS X-joints were investigated at four elevated temperatures, including 400°C, 500°C, 600°C and 1000°C. The FE analyses of parametric specimens were performed using mechanical properties at elevated temperatures predicted from the constitutive material model proposed by Li and Young [51] for cold-formed S900 steel grade tubular members. Fig. 8 presents the stress-strain curves at 400°C, 500°C, 600°C and 1000°C. Table 1 presents the mechanical properties at 400°C, 500°C, 600°C and 1000°C, which include Young's modulus (E_0), 0.2% proof stress ($\sigma_{0.2}$), ultimate strength (σ_u) and ultimate strain (ε_u). With the exception of mechanical properties at elevated temperatures, all FE modelling techniques described in Section 5 of this paper were used to perform the numerical parametric study on cold-formed S900 steel grade RHS X-joints at elevated temperatures.

In order to gain a broad understanding of various critical factors affecting the static behaviour of RHS X-joints at elevated temperatures, the database was widened by performing a comprehensive numerical parametric study. In total, 756 RHS X-joint FE specimens were analysed in the parametric study, including 189 FE specimens corresponding to each elevated temperature. The validity ranges of critical geometric parameters were purposefully widened beyond the present limitations set by EC3 [11] and CIDECT [12]. Table 2 presents the overall ranges of various critical parameters considered in this investigation. In the parametric study, the values of cross-section width and depth of braces and chords of FE specimens varied from 30 mm to 600 mm, while the wall thickness of braces and chords varied from 2.25 mm to 12.5 mm. The external corner radii of braces and chords (R_1 and R_0) conformed to commercially produced HSS members [62]. In this study, R_1 and R_0 were kept as $2t$ for $t \leq 6$ mm, $2.5t$ for $6 < t \leq 10$ mm and $3t$ for $t > 10$ mm, which in turn also met the limits detailed in EN [61]. The lengths of braces (L_1) were equal to two times the maximum of b_1 and h_1, and the lengths of chords (L_0) were equal to h_1 + $4h_0$, which in turn were consistent with the experimental and numerical investigations carried out by the authors [3,10].

For meshing along the longitudinal and transverse directions of tubular members, seedings were approximately spaced at the minimum of b/30 and h/30. Overall, the adopted mesh sizes of parametric FE specimens varied from 3 to 12 mm. On the other hand, the seeding interval of weld parts of parametric FE specimens reciprocated the seeding interval of their corresponding brace parts. For precise replication of RHS curvatures, the corner portions of RHS members were split into ten parts. For RHS members with $t \leq 6$ mm, no divisions were made along the wall thickness of the parametric FE specimens. However, for RHS members with $t > 6$ mm, the wall thickness of parametric FE specimens was divided into two layers. With regard to the weld modelling, FW was modelled for FE specimens with $\beta \leq 0.80$. However, for FE specimens with $\beta > 0.80$, GW and FW were respectively modelled along the longitudinal and transverse directions of the chords. Following the prequalified tubular joint details given in AWS D1.1M [63], the leg size of FW was designed as 1.5 times the minimum of t_1 and t_0, which was consistent with the numerical investigations performed at room temperature and post-fire conditions [10,37]. The weld parts were also assigned the mechanical properties determined from the constitutive material model proposed by Li and Young [51]. In addition, the flat part of chord web (i.e. h_0-$2R_0$) of equal-width RHS X-joint was outward bulged at its centre by $0.015b_0$, as shown in Fig. 3.

6.2. Failure modes

Overall, three types of failure modes were identified in this numerical investigation. First, failure of RHS X-joints by chord flange yielding, which was termed as chord face failure and denoted by the letter 'F' in this study. Second, failure of RHS X-joints due to buckling of chord webs, which was termed as chord side wall failure and denoted by the letter 'S' in this study. Third, failure of RHS X-joints due to the combination of chord face and chord side wall failures, which was named as combined failure and denoted by 'F+S' in this study. It is important to note that these failure modes were defined corresponding to the $N_{f,T}$, which in turn was computed by combinedly considering the peak and $0.03b_0$ limit loads, whichever occurred earlier in the $N_{f,T}$ vs u curve. The RHS X-joints were failed by the F mode, when the $N_{f,T}$ was determined using the $0.03b_0$ limit criterion. The applied load of RHS X-joint failed by the F mode was monotonically increasing. In this investigation, RHS X-joints were failed by the F mode when $0.30 \leq \beta \leq 0.75$. On the other hand, RHS X-joints were failed by the S mode when β=1.0. For RHS X-joints that failed by the F+S mode, the $N_{f,T}$ vs u curve exhibited a clear ultimate load. Additionally, evident deformations of chord flange, chord webs and chord corner regions were noticed in the specimens that failed by the F+S mode. The specimens were failed by the F+S mode in this investigation when $0.80 \leq \beta \leq 0.90$. Moreover, none of the specimens was failed by the global buckling of braces. Figs. 9 to 11 present the variations of $N_{f,T}$ vs u curves for typical RHS X-joints that failed by the F, F+S and S failure modes corresponding to all the four investigated elevated temperatures, respectively.

7. Design rules

Currently, design rules for predicting the residual strengths of tubular joints at elevated temperatures are not given in any of the international code and guide. In order to examine the suitability of EC3 [11] and CIDECT [12] design provisions for cold-formed S900 steel grade RHS X-joints at elevated temperatures, in this study, the nominal resistances from design equations given in EC3 [11] and CIDECT [12] ($N_{E,T}$ and $N_{C,T}$) were determined using the mechanical properties shown in Table 1. The design rules given in EC3 [11] and CIDECT [12] are shown below:

Chord face failure (*$\beta \leq 0.85$*)

EC3 [11]:

$$N_{E,T} = C_f \left[k_n \frac{f_{y0,T} t_0^2}{(1-\beta)\sin\theta_1} \left(\frac{2\eta}{\sin\theta_1} + 4\sqrt{1-\beta} \right) / \gamma_{M5} \right] \tag{1}$$

CIDECT [12]:

$$N_{C,T} = C_f \left[Q_f \frac{f_{y0,T} t_0^2}{\sin\theta_1} \left(\frac{2\eta}{(1-\beta)\sin\theta_1} + \frac{4}{\sqrt{1-\beta}} \right) \right] \tag{2}$$

Chord side wall failure (*$\beta = 1.0$*)

EC3 [11]:

$$N_{E,T} = C_f \left[k_n \frac{f_{b,T} t_0}{\sin\theta_1} \left(\frac{2h_1}{\sin\theta_1} + 10t_0 \right) / \gamma_{M5} \right] \tag{3}$$

CIDECT [12]:

$$N_{C,T} = C_f \left[Q_f \frac{f_{k,T} t_0}{\sin\theta_1} \left(\frac{2h_1}{\sin\theta_1} + 10t_0 \right) \right] \tag{4}$$

The nominal resistances from EC3 [11] were determined using the 0.2% proof stress at elevated temperatures and partial safety factor (γ_{M5}) equal to 1.0. In addition, a material factor (C_f) equal to 0.80 was adopted as per EC3 [64]. On the other hand, CIDECT [12] uses the minimum of 0.2% proof stress and 0.80 times the corresponding ultimate strength for joint resistance calculation. Moreover, design provisions given in CIDECT [12] recommend the use of C_f equal to 0.90 for tubular joints with steel grade exceeding S355. Unlike EC3 [11], CIDECT [12] uses different values of partial safety factors (γ_M) for different tubular joints and their corresponding failure modes, which are given in IIW [65]. However, their effects are implicitly included inside the CIDECT [12] design provisions. Thus, nominal resistances from CIDECT [12] were calculated using γ_M equal to 1.0 and 1.25 for chord face failure and chord side wall failure, respectively. In Eqs. (1) to (4), chord stress functions are denoted by k_n and Q_f (in this investigation, the values of k_n and Q_f were adopted as 1.0), yield stress of chord member at elevated temperatures is denoted by $f_{y0,T}$, the parameter η is equal to h_1/b_0, chord side wall buckling stresses at elevated temperatures are denoted by $f_{b,T}$ and $f_{k,T}$, and the angle between brace and chord is denoted by θ_1 (in degrees).

8. Reliability analysis

In order to examine the reliability of existing and proposed design equations, a reliability study was performed as per AISI S100 [66]. In this investigation, a lower bound value of 2.50 was defined as the target reliability index (β_0). Therefore, when $\beta_0 \geq 2.50$, the design equation was treated as reliable in this study. In the reliability analysis method, the dead load (DL)-to-live load (LL) ratio equal to 0.20 was used to compute the calibration coefficient (C_ϕ). Referring to AISI S100 [66], the values of mean and COV of material factor were adopted as 1.10 and 0.10, respectively. On the other hand, the values of mean and COV of fabrication factor were adopted as 1.00 and 0.10, respectively. The resistance factor required to convert nominal resistance to design resistance was denoted by ϕ. The mean value of the ratios of FE joint resistances-to-nominal resistances predicted from existing and proposed design equations was denoted by P_m, while the corresponding COV was denoted by V_P. The correction factor (C_P) given in AISI S100 [66] was used to incorporate the effect of the number of data under consideration. To evaluate the reliability levels of EC3 [11] design provisions, the DL and LL were combined as 1.35DL + 1.5LL [67], and thus, the calculated value of C_ϕ was 1.463. Further, to examine the reliability levels of CIDECT [12] design provisions as well as proposed design rules, the DL and LL were combined as 1.2DL + 1.6LL [68], and therefore, the calculated value of C_ϕ was 1.521.

9. Comparisons between residual joint resistances and nominal resistances

For different observed failure modes, the overall summary of comparisons between $N_{f,T}$ and nominal resistances predicted from design rules given in EC3 [11] and CIDECT [12] using mechanical properties at elevated temperatures are shown in Tables 3 to 5. The comparisons are also graphically shown in Figs. 12 to 14 for different failure modes. Table 3 and Fig. 12 present the comparisons for RHS X-joint specimens that failed by the F mode. The comparison results proved that using the mechanical properties at elevated temperatures, the design rules given in EC3 [11] and CIDECT [12] are quite conservative but scattered and unreliable for the design of cold-formed S900 steel grade RHS X-joints. In Fig. 12, generally, RHS X-joint specimens with small values of β and η ratios and large values of 2γ ratio lie below the unit slope line (i.e. $y=x$). For such specimens, the joint resistance corresponding to the $0.03b_0$ limit was not sufficient to cause the yielding of chord flanges. On the contrary, the yield line theory has been used to derive the existing design equation for RHS X-joint specimens that failed by the F mode [11,12]. Consequently, $N_{f,T}$ of RHS X-joint specimens became smaller than the corresponding nominal resistances predicted from design rules given in EC3 [11] and CIDECT [12] using mechanical properties at elevated temperatures. As a result, such cases fall below the line of unit slope. The data above the line of unit slope, on the other hand, indicate RHS X-joint specimens with medium to large values of β and η ratios and small values of 2γ ratio.

The summary of comparison results of RHS X-joint specimens that failed by the F+S mode at elevated temperatures are shown in Table 4 and Fig. 13. It can be noticed that using mechanical properties at elevated temperatures, the current design provisions given in EC3 [11] and CIDECT [12] are found to be demonstrated to be largely conservative. The data above the unit slope line in Fig. 13 typically represent RHS X-joints with large values of β ratio and small values of 2γ and h_0/t_0 ratios. As the β ratio of RHS X-joint failed by the F+S mode increased, the brace member gradually approached the chord corner regions. Consequently, the $N_{f,T}$ of such joints increased due to the enhanced rigidity of chord corner regions. On the other hand, the corresponding increase in nominal resistances predicted from design rules given in EC3 [11] and CIDECT [12] was lower than the $N_{f,T}$ of RHS X-joints. Subsequently, such data fall above the line of unit slope in Fig. 13. Table 5 and Fig. 14 present the comparison results of RHS X-joint specimens that failed by the S mode. The existing design rules, using mechanical properties at elevated temperatures, apparently provided very conservative predictions and were accompanied by significantly large values of COV. However, design rules are unreliable. The EC3 [11] and CIDECT [12] design provisions for the S failure mode considered chord webs as pin-ended columns, which resulted in very conservative predictions as h_0/t_0 ratio increased.

10. Proposed design rules

Using two design methods, named as proposal-1 and -2, design rules are proposed in this study for different failure modes of the investigated cold-formed S900 steel grade RHS X-joints at elevated temperatures (T). The design rules proposed in both the methods (i.e. proposal-1 and -2) were based on the design equations proposed by Pandey and Young [10] for CFHSS RHS X-joints at room temperature. In the first design method (i.e. proposal-1), the mechanical properties at room temperature used in the design equations proposed by Pandey and Young [10] are replaced with the mechanical properties at elevated temperatures. In addition, a correction factor (Ω) based on the elevated temperatures is also applied on the proposed design rules. On the other hand, in the second design method (i.e. proposal-2), only a correction factor based on the elevated temperatures is applied on the design rules proposed by Pandey and Young [10] at room temperature. Therefore, design equations under proposal-1 can predict the $N_{f,T}$ of RHS X-joints when mechanical properties at elevated temperatures are available. However, design equations under proposal-2 can predict the $N_{f,T}$ only using the elevated temperatures. It should be noted that the design rules proposed in this study are valid for 400°C $\leq T \leq$ 1000°C. In this study, the validity ranges of important parameters influencing the static behaviour of RHS X-joints were extended beyond their existing limits given in EC3 [11] and CIDECT [12]. Furthermore, as welds were modelled in all FE specimens, the influence of welds was implicitly included in the proposed design rules. In order to obtain design resistances (N_d), the proposed nominal resistances (N_{pn1} and N_{pn2}) in the following sub-sections of this paper shall be multiplied by their correspondingly recommended resistance factors (ϕ), i.e. $N_d = \phi$ (N_{pn1} or N_{pn2}).

10.1. RHS X-joints failed by F mode

The design equations proposed under proposal-1 and -2 for RHS X-joints failed by the F mode at elevated temperatures are as follows:

Proposal-1:

Using mechanical properties at elevated temperatures (T):

$$N_{pn1} = (0.001T + 0.6)\left[f_{y0,T} t_0^2 \left(\frac{28\beta + 7\eta - 7}{1 + 0.01(2\gamma)} \right) \right] \tag{5}$$

Proposal-2:

Using mechanical properties at room temperature and elevated temperature correction factor (Ω):

$$N_{pn2} = \Omega \left[f_{y0} t_0^2 \left(\frac{28\beta + 7\eta - 7}{1 + 0.01(2\gamma)} \right) \right] \tag{6}$$

where

$$\Omega = \begin{cases} 1.58 - 2\times10^{-3}T & \text{for} \quad 400°\text{C} \le T \le 600°\text{C} \\ 0.9 - 8.65\times10^{-4}T & \text{for} \quad 600°\text{C} < T \le 1000°\text{C} \end{cases} \tag{7}$$

The Eqs. (5) and (6) are valid for $0.30 \le \beta \le 0.75$, $16.6 \le 2\gamma \le 50$, $16.6 \le h_0/t_0 \le 50$, $0.3 \le \eta \le 1.2$ and $0.75 \le \tau \le 1.0$. As shown in Table 3, the P_m and V_p of proposal-1 (i.e. Eq. (5)) are 1.00 and 0.177, respectively, while the P_m and V_p of proposal-2 (i.e. Eq. (6)) are 1.02 and 0.160, respectively. For Eqs. (5) and (6), ϕ equal to 0.75 and 0.80 are recommended, resulting in β_0 equal to 2.61 and 2.53, respectively. Thus, Eqs. (5) and (6) must be multiplied by ϕ equal to 0.75 and 0.80 to obtain their corresponding design resistances (N_d), respectively. The comparisons of $N_{f,T}$ of RHS X-joint specimens with nominal resistances predicted from design equations given in EC3 [11], CIDECT [12] as well as predictions from proposal-1 and -2 are graphically presented in Fig. 12. Compared to the design provisions given in EC3 [11] and CIDECT [12], the proposed equations (Eqs. (5) and (6)) are relatively more accurate, less scattered and reliable.

10.2. RHS X-joints failed by F+S mode

The design equations proposed under proposal-1 and -2 for RHS X-joints failed by the F+S mode at elevated temperatures are as follows:

Proposal-1:

Using mechanical properties at elevated temperatures (T):

$$N_{pn1} = (0.0009T + 0.6)\left[f_{y0,T} t_0^2 \left(\frac{60\beta + 8\eta - 38}{0.9 + 0.003(2\gamma)} \right) \right] \tag{8}$$

Proposal-2:

Using mechanical properties at room temperature and elevated temperature correction factor (Ω):

$$N_{pn2} = \Omega \left[f_{y0} t_0^2 \left(\frac{60\beta + 8\eta - 38}{0.9 + 0.003(2\gamma)} \right) \right] \tag{9}$$

where

$$\Omega = \begin{cases} 1.61 - 2.1\times10^{-3} T & \text{for} \quad 400°\text{C} \le T \le 600°\text{C} \\ 0.83 - 8\times10^{-4} T & \text{for} \quad 600°\text{C} < T \le 1000°\text{C} \end{cases} \tag{10}$$

The Eqs. (8) and (9) are valid for $0.80 \le \beta \le 0.90$, $16.6 \le 2\gamma \le 50$, $16.6 \le h_0/t_0 \le 50$, $0.6 \le \eta \le 1.2$ and $0.75 \le \tau \le 1.0$. As shown in Table 4, the P_m and V_p of proposal-1 (i.e. Eq. (8)) are 1.02 and 0.189, respectively, while the P_m and V_p of proposal-2 (i.e. Eq. (9)) are 1.06 and 0.179, respectively. For Eqs. (8) and (9), ϕ equal to 0.75 and 0.80 are recommended, resulting in β_0 equal to 2.60 and 2.56, respectively. Thus, Eqs. (8) and (9) must be multiplied by ϕ equal to 0.75 and 0.80 to obtain their corresponding design resistances (N_d), respectively. The comparisons of $N_{f,T}$ of RHS X-joint specimens with nominal resistances predicted from design equations given in EC3 [11], CIDECT [12] as well as predictions from proposal-1 and -2 are graphically presented in Fig. 13. Compared to the design provisions given in EC3 [11] and CIDECT [12], the proposed equations (Eqs. (8) and (9)) are relatively more accurate, less scattered and reliable.

10.3. RHS X-joints failed by S mode

The design equations proposed under proposal-1 and -2 for RHS X-joints failed by the S mode at elevated temperatures are as follows:

Proposal-1:

Using mechanical properties at elevated temperatures (T):

$$N_{pn1} = \begin{cases} N_1 = (1.4 - 0.0009T) \left[\frac{f_{k,T}(2b_w t_0)}{(0.4\eta + 2)} \left(\frac{1.4 - 0.05(2\gamma) + 2.4\tau}{2e^{-0.05\left(\frac{h_0}{t_0}\right)}} \right) \right] & \text{for} \quad 400°\text{C} \le T \le 600°\text{C} \\ N_2 = 1.75 \left(e^{-0.03\frac{h_0}{t_0}} \right) \left[\frac{f_{k,T}(2b_w t_0)}{(0.4\eta + 2)} \left(\frac{1.4 - 0.05(2\gamma) + 2.4\tau}{2e^{-0.05\left(\frac{h_0}{t_0}\right)}} \right) \right] & \text{for} \quad T = 1000°\text{C} \\ \text{Linear interpolation between } N_1 \text{ and } N_2 & \text{for} \quad 600°\text{C} < T < 1000°\text{C} \end{cases} \tag{11}$$

Proposal-2:

Using mechanical properties at room temperature and elevated temperature correction factor (Ω):

$$N_{pn2} = \Omega\left[\frac{f_k\left(2b_w t_0\right)}{\left(0.4\eta+2\right)}\left(\frac{1.4-0.05\left(2\gamma\right)+2.4\tau}{2e^{-0.05\left(\frac{h_0}{t_0}\right)}}\right)\right] \tag{12}$$

where

$$\Omega = \begin{bmatrix} 1.74-2.3\times10^{-3}T & \text{for} \quad 400°\text{C} \le T \le 600°\text{C} \\ 0.84-8\times10^{-4}T & \text{for} \quad 600°\text{C} < T \le 1000°\text{C} \end{bmatrix} \tag{13}$$

The Eqs. (11) and (12) are valid for β = 1.0, $16.6 \le 2\gamma \le 50$, $10 \le h_0/t_0 \le 60$, $0.6 \le \eta \le 1.2$ and $0.75 \le \tau \le 1.25$. As shown in Table 5, the P_m and V_p of proposal-1 (i.e. Eq. (11)) are 1.01 and 0.185, respectively, while the P_m and V_p of proposal-2 (i.e. Eq. (12)) are 1.06 and 0.188, respectively. For Eqs. (11) and (12), ϕ equal to 0.75 and 0.80 are recommended, resulting in β_0 equal to 2.58 and 2.51, respectively. Thus, Eqs. (11) and (12) must be multiplied by ϕ equal to 0.75 and 0.80 to obtain their corresponding design resistances (N_d), respectively. The comparisons of $N_{f,T}$ of RHS X-joint specimens with nominal resistances predicted from design equations given in EC3 [11], CIDECT [12] as well as predictions from proposal-1 and -2 are graphically presented in Fig. 14. Compared to the design provisions given in EC3 [11] and CIDECT [12], the proposed equations (Eqs. (11) and (12)) are relatively more accurate, less scattered and reliable. The buckling curve 'a' of EC3 [69] was used to determine the $f_{k,T}$ and f_k in Eqs. (11) and (12). Moreover, the flat portions of chord side walls were equal to h_0-2R_0. Additionally, instead of assuming pin-ended boundary conditions for the flat portions of chord side walls, the effective length of the chord side wall column was determined using a factor equal to 0.85. Therefore, in this study, the effective lengths of the flat portions of chord side walls were equal to 0.85×(h_0-2R_0). The definition of the width of the chord web column (b_w) was identical to that given in EC3 [11] and CIDECT [12].

It is important to note that for RHS X-joint specimens with $0.75 < \beta < 0.80$ and $0.90 < \beta < 1.0$, the nominal resistances under proposal-1 can be obtained by performing a linear interpolation between Eqs. (5) & (8) and Eqs. (8) & (11), respectively. Similarly, for proposal-2, the nominal resistances of RHS X-joint specimens with $0.75 < \beta < 0.80$ and $0.90 < \beta < 1.0$ can be obtained by performing a linear interpolation between Eqs. (6) & (9) and Eqs. (9) & (12), respectively.

11. Conclusions

The static performance of cold-formed S900 steel grade square and rectangular hollow section (SHS and RHS) X-joints was numerically investigated at elevated temperatures (T). The residual static strengths of SHS and RHS X-joints undergoing axial compression loads were determined at 400°C, 500°C, 600°C and 1000°C. A total of 756 FE specimens were analysed in the parametric study, where the validity ranges of important geometric parameters exceeded the limits prescribed in EC3 [11] and CIDECT [12]. The mechanical properties at elevated temperatures predicted from the constitutive stress-strain model proposed by Li and Young [51] were used in the parametric study. The welds were modelled in all RHS X-joint specimens. Overall, RHS X-joints were failed by three failure modes, including chord face failure (F), chord side wall failure (S), and a combination of these two failure modes, i.e. combined failure (F+S) mode. The nominal resistances predicted from design rules given in EC3 [11] and CIDECT [12], using mechanical properties at elevated temperatures, were compared with the resistances of RHS X-joints investigated in this study. Overall, it has been demonstrated that the design rules given in EC3 [11] and CIDECT [12] are quite conservative, and predictions are largely scattered. Therefore, using the two design methods, accurate, less scattered and reliable design rules are proposed in this study for the design of cold-formed steel RHS X-joints made of S900 steel grade at elevated temperatures. The proposed design equations are valid for temperatures ranging from 400°C to 1000°C.

Acknowledgement

The work described in this paper was fully supported by a grant from the Research Grants Council of the Hong Kong Special Administrative Region, China (Project No. 17210218).

References

[1] Pandey M, Young B. Tests of cold-formed high strength steel tubular T-joints. Thin-Walled Structures, 2019;143:106200.

[2] Pandey M, Young B. Compression capacities of cold-formed high strength steel tubular T-joints. Journal of Constructional Steel Research, 2019;162:105650.

[3] Pandey M and Young B. Structural performance of cold-formed high strength steel tubular X-Joints under brace axial compression. Engineering Structures, 2020; 208:109768.

[4] Pandey M and Young B. Ultimate Resistances of Member-Rotated Cold-Formed High Strength Steel Tubular T-Joints under Compression Loads, Engineering Structures, 2021;244:112601.

[5] Pandey M and Young B. Experimental Investigation on Stress Concentration Factors of Cold-formed High Strength Steel Tubular X-Joints, Engineering Structures, 2021;243:112408.

[6] Pandey M, Chung KF and Young B. Design of cold-formed high strength steel tubular T-joints under compression loads. Thin-Walled Structures, 2021;164:107573.

[7] Pandey M, Chung KF and Young B. Numerical investigation and design of fully chord supported tubular T-joints. Engineering Structures, 2021;239:112063.

[8] Lan X, Chan TM and Young B. Structural behaviour and design of high strength steel RHS X-joints. Engineering Structures, 2019; 200:109494.

[9] Lan X, Chan TM and Young B. Testing, finite element analysis and design of high strength steel RHS T-joints. Engineering Structures, 2021; 227:111184.

[10] Pandey M and Young B. Static Performance and Design of Cold-formed High Strength Steel Rectangular Hollow Section X-Joints, Engineering Structures (in press).

[11] Eurocode 3 (EC3), Design of Steel Structures-Part 1-8: Design of Joints, EN 1993-1-8, European Committee for Standardization, CEN, Brussels, Belgium, 2005.

[12] Packer JA, Wardenier J, Zhao XL, Vegte GJ van der, Kurobane Y. Design guide for rectangular hollow section (RHS) joints under predominantly static loading. Comite´ International pour le Developpement et l'Etude de la Construction TuECbulaire (CIDECT), Design Guide No. 3, 2nd edn., LSS Verlag, Dortmund, Germany, 2009.

[13] Lan X and Huang Y. Structural design of cold-formed stainless steel tubular X-and T-joints at elevated temperatures. Thin-Walled Structures, 2016; 108:270-279.

[14] Lan X, Huang Y, Chan TM and Young B. Static strength of stainless steel K-and N-joints at elevated temperatures. Thin-Walled Structures, 2018;122:501-509.

[15] Feng R. and Young B. Design of cold-formed stainless steel tubular joints at elevated temperatures. Engineering Structures, 2012;35:188-202.

[16] Chen J, Young B. Stress-strain curves for stainless steel at elevated temperatures. Engineering Structures, 2006;28(2):229–39.

[17] Nassiraei H, Lotfollahi-Yaghin MA, Neshaei SA, Zhu L. Structural behavior of tubular X-joints strengthened with collar plate under axially compressive load at elevated temperatures, Marine Structures, 2018;61:46–61.

[18] Shao Y, Haicheng Z, Dongping Y. Discussion on two methods for determining static strength of tubular T-joints at elevated temperature, Advances in Structural Engneering; 2017;20 (5):704–721.

[19] Dodaran NA, Ahmadi H, Lotfollahi-Yaghin MA. Static strength of axially loaded tubular KT-joints at elevated temperatures: study of geometrical effects and parametric formulation, Marine Structures, 2018;61:282–308.

[20] Chen C, Shao YB, Yang J. Study on fire resistance of circular hollow section (CHS) T-joint stiffened with internal rings, Thin-Walled Structures, 2015;92:104–114.

[21] Gao F, Guan XQ, Zhu HP, Liu XN. Fire resistance behaviour of tubular T-joints reinforced with

collar plates. Journal of Constructional Steel Research, 2015; 115:106–120.
[22] Gao F, Zhu H, Liang H, Tian Y. Post-fire residual strength of steel tubular T-joint with concrete-filled chord. Journal of Constructional Steel Research, 2017; 139:327–338.
[23] Cheng C, Shao Y, Yang J. Experimental and numerical study on fire resistance of circular tubular T-joints. Journal of Constructional Steel Research, 2013; 85:24–39.
[24] Tan KH, Fung TC and Nguyen MP. Structural behavior of CHS T-Joints subjected to brace axial compression in fire conditions. Journal of Structural Engineering, 2013; 139(1):73-84.
[25] Fung TC, Tan KH and Nguyen MP. Structural behavior of CHS T-joints subjected to static in-plane bending in fire conditions. Journal of Structural Engineering, 2016;142(3):04015155.
[26] Ozyurt E, Wang YC and Tan KH. Elevated temperature resistance of welded tubular joints under axial load in the brace member. Engineering Structures, 2014;59:574-586.
[27] Ozyurt E and Wang YC. Resistance of axially loaded T-and X-joints of elliptical hollow sections at elevated temperatures–a finite element study, Structures, 2018;14:15-31.
[28] He S, Shao Y, Zhang H and Wang Q. Parametric study on performance of circular tubular K-joints at elevated temperature. Fire safety journal, 2015;71:174-186.
[29] Nguyen MP, Fung TC and Tan KH. An experimental study of structural behaviours of CHS T-joints subjected to brace axial compression in fire condition. Tubular Structures XIII, Hong Kong, 2010:725-732.
[30] Nguyen MP, Tan KH and Fung TC. Numerical models and parametric study on ultimate strength of CHS T-joints subjected to brace axial compression under fire condition. Tubular Structures XIII, Hong Kong, 2010:733-740.
[31] Yu W, Zhao J, Luo H, Shi J and Zhang D. Experimental study on mechanical behavior of an impacted steel tubular T-joint in fire. Journal of Constructional Steel Research, 2011; 67(9):1376-1385.
[32] Jin M, Zhao J, Chang J and Zhang D. Experimental and parametric study on the post-fire behavior of tubular T-joint. Journal of Constructional Steel Research, 2012; 70:93-100.
[33] Liu M, Zhao J and Jin M. An experimental study of the mechanical behavior of steel planar tubular trusses in a fire. Journal of Constructional Steel Research, 2010; 66(4):504-511.
[34] Yu W, Zhao J, Luo H, Shi J and Zhang D. Experimental study on mechanical behavior of an impacted steel tubular T-joint in fire. Journal of Constructional Steel Research, 2011; 67(9):1376-1385.
[35] Xu J, Zhao J, Song Z and Liu M. Prediction of ultimate bearing capacity of Tubular T-joint under fire using artificial neural networks. Safety science, 2012; 50(7):1495-1501.
[36] Abaqus/Standard. Version 6.17. USA: K. a. S. Hibbit; 2017.
[37] Pandey M and Young B. RHS-to-RHS Cold-formed S960 Steel Fire Exposed X-Joints: Structural Behaviour and Design, Thin-Walled Structures (under review).
[38] Ozyurt E and Wang YC. A numerical investigation of static resistance of welded planar steel tubular joints under in-plane and out-of-plane bending at elevated temperatures. Engineering Structures, 2019; 199:109622.
[39] Nassiraei H, Mojtahedi A, Lotfollahi-Yaghin MA and Zhu L. Capacity of tubular X-joints reinforced with collar plates under tensile brace loading at elevated temperatures. Thin-Walled Structures, 2019; 142:426-443.
[40] Azari-Dodaran N, Ahmadi H, Zhu L and Li P. Experimental and numerical study of the ultimate load for collar-plate-reinforced tubular K-joints at fire-induced elevated temperatures. Ships and Offshore Structures, 2022;17(5):1159-1177.
[41] Ozyurt E. Finite element study on axially loaded reinforced Square Hollow Section T-joints at elevated temperatures. Thin-Walled Structures, 2020; 148:106582.

[42] Lan X, Wang F, Luo Z, Liu D, Ning C and Xu X. Joint strength reduction factor of internally ring-stiffened tubular joints at elevated temperatures. Advances in Structural Engineering, 2016; 19(10):1650-1660.

[43] Azari-Dodaran N and Ahmadi H. Numerical study on the ultimate load of offshore two-planar tubular KK-joints at fire-induced elevated temperatures. Journal of Marine Engineering & Technology, 2022;21(4):205-233.

[44] Dodaran NA, Ahmadi H and Lotfollahi-Yaghin MA. Parametric study on structural behavior of tubular K-joints under axial loading at fire-induced elevated temperatures. Thin-Walled Structures, 2018; 130:467-486.

[45] Ozyurt E and Wang YC. Resistance of T- and K-joints to tubular members at elevated temperatures. In Proc of Applications of Structural Fire Engineering, Wald, Burgess, Horova, Jana, Jirku (eds), CTU Publishing House, Prague, 2013:179-185.

[46] Ozyurt E and Wang YC. Resistance of welded tubular T-and X-joints made of high strength steel at elevated temperatures. In Proceedings of the 17th international symposium on tubular structures, 2019:9-12.

[47] Azari-Dodaran N and Ahmadi H. Static behavior of offshore two-planar tubular KT-joints under axial loading at fire-induced elevated temperatures. Journal of Ocean Engineering and Science, 2019; 4(4):352-372.

[48] Wang YC and Ozyurt E. Static resistance of axially loaded multiplanar gap KK-joints of Circular Hollow sections at elevated temperatures. Engineering Structures, 2021; 229:111676.

[49] Nassiraei H. Static strength of tubular T/Y-joints reinforced with collar plates at fire induced elevated temperature. Marine Structures, 2019; 67:102635.

[50] Azari-Dodaran N and Ahmadi H. Structural behavior of right-angle two-planar tubular TT-joints subjected to axial loadings at fire-induced elevated temperatures. Fire Safety Journal, 2019; 108:102849.

[51] Li HT and Young B. Cold-formed high strength steel SHS and RHS beams at elevated temperatures. Journal of Constructional Steel Research, 2019; 158:475-485.

[52] Li HT and Young B. Material properties of cold-formed high strength steel at elevated temperatures. Thin-Walled Structures, 2017;115:289-299.

[53] Pandey M and Young B. Post-Fire Behaviour of Cold-Formed High Strength Steel Tubular T- and X-Joints, Journal of Constructional Steel Research, 2021;186:106859.

[54] ISO-834. Fire-resistance tests-Elements of Building Construction-Part 1-General requirements. ISO 834-1, International Organization of Standards, 1999.

[55] Crockett P. Finite element analysis of welded tubular connections. PhD Thesis, University of Nottingham, 1994.

[56] Pandey M, Young B. Post-fire Mechanical Response of High Strength Steels. Thin-Walled Structures, 164 (2021) 107606.

[57] Ma JL, Chan TM and Young B. Design of cold-formed high strength steel tubular beams. Engineering Structures, 2017;151:432-443.

[58] Li QY and Young B. Design of cold-formed steel built-up open section members under combined compression and bending. Thin-Walled Structures, 2022;172:108890.

[59] Li HT and Young B. Cold-formed stainless steel RHS members undergoing combined bending and web crippling: Testing, modelling and design. Engineering Structures, 2022;250:113466.

[60] Garifullin M, Bronzova MK, Heinisuo M, Mela K and Pajunen S. Cold-formed RHS T joints with initial geometrical imperfections. Magazine of Civil Engineering, 2018,82(6).

[61] EN 10219-2. Cold formed welded structural hollow sections of non-alloy and fine grain steels-Part 2: Tolerances, dimensions and sectional properties. European Committee for

Standardization (CEN), Brussels, Belgium; 2006.
[62] SSAB. Strenx Tube 960 MH. Data Sheet 2043, Sweden, 2017.
[63] AWS D1.1/D1.1M, Structural Welding Code – Steel, American Welding Society (AWS), Miami, USA, 2020.
[64] Eurocode 3 (EC3), Design of steel structures. Part 1-12: Additional rules for the extension of EN 1993 up to steel grades S700, EN 1993-1-12, European Committee for Standardization, CEN, Brussels, Belgium, 2007.
[65] IIW Doc. XV-1402-12 and IIW Doc. XV-E-12-433. Static design procedure for welded hollow section joints – Recommendations. International Institute of Welding, Paris, France, 2012.
[66] AISI S100. North American Specification for the design of cold-formed steel structural members. American Iron and Steel Institute (AISI), Washington, D.C., USA, 2016.
[67] EN 1990. Eurocode: Basis of structural design. European Committee for Standardization (CEN), Brussels, Belgium, 2002.
[68] ASCE/SEI 7. Minimum Design Loads for Buildings and Other Structures. American Society of Civil Engineers (ASCE), New York, USA, 2016.
[69] Eurocode 3 (EC3), Design of Steel Structures–Part 1-1: General Rules and Rules for Buildings, EN 1993-1-1, European Committee for Standardization (CEN), Brussels, Belgium, 2005.

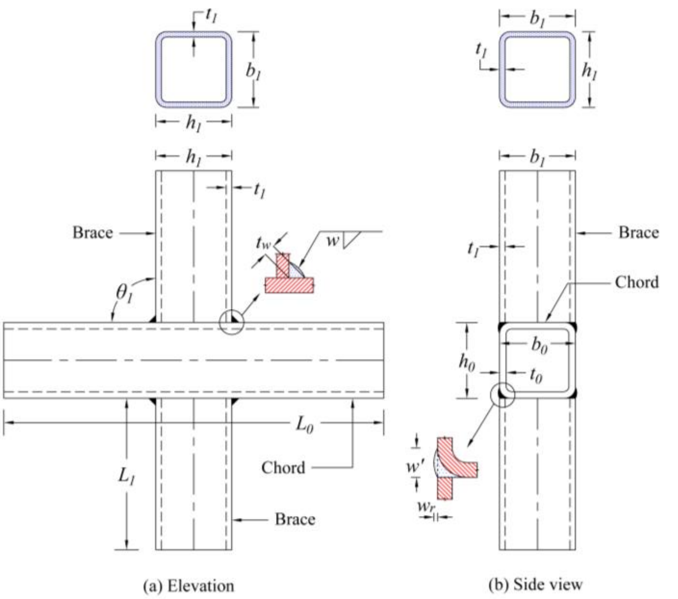

Fig. 1. Representations of geometric notations for RHS X-joint.

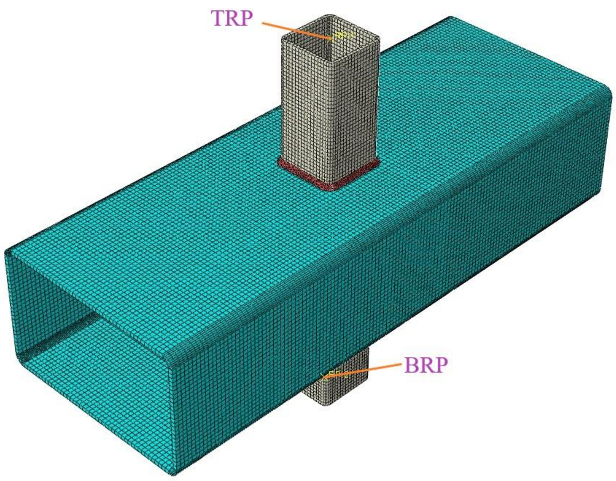

(a) Typical FE model of RHS X-joint with small β value (β=0.30).

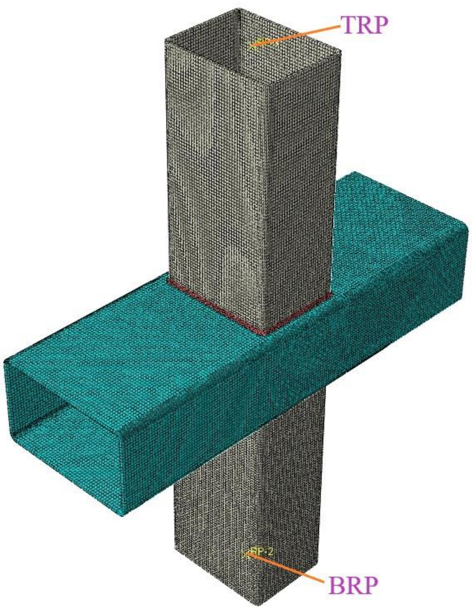

(b) Typical FE model of RHS X-joint with medium β value (β=0.80).

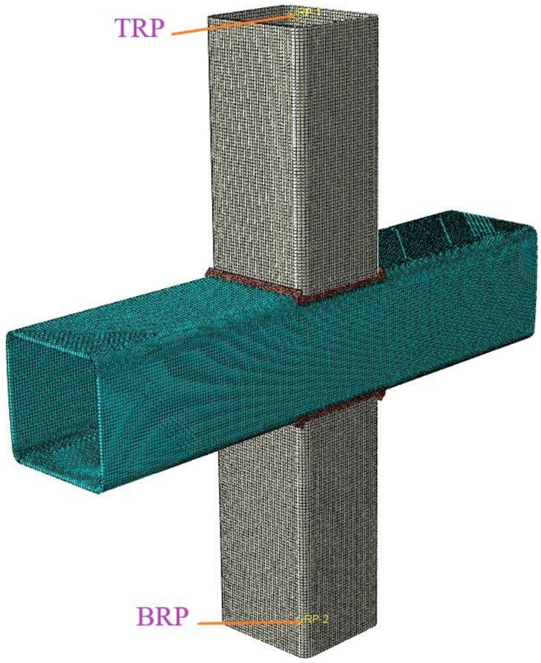

(c) Typical FE model of equal-width RHS X-joint (β=1.0).

Fig. 2. Typical FE models of RHS X-joints.

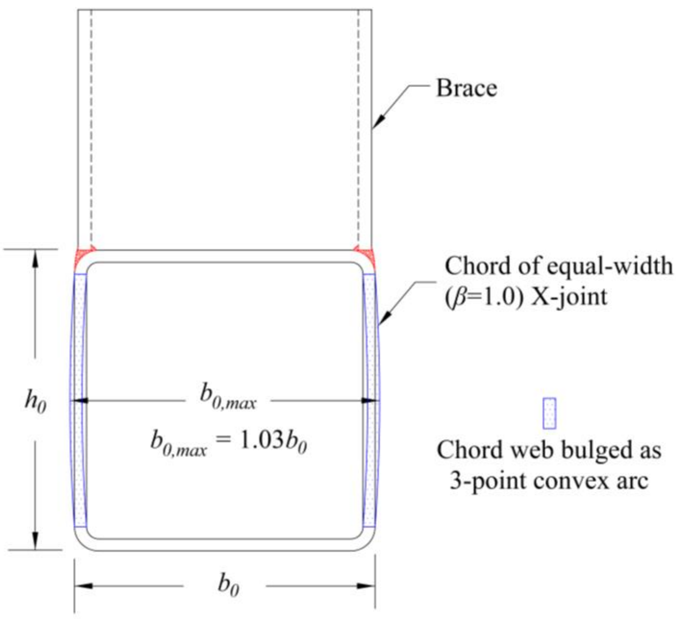

Fig. 3. Initial geometric imperfection modelled in chord webs of equal-width RHS X-joint.

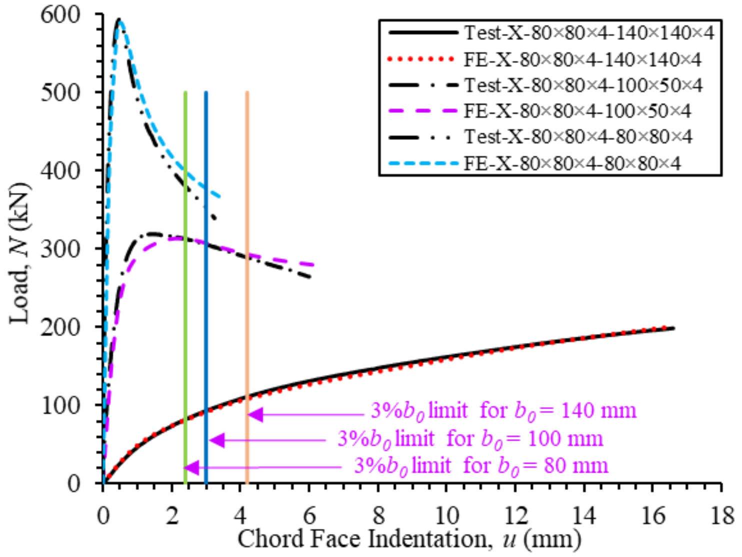

(a) Load vs chord face indentation curves.

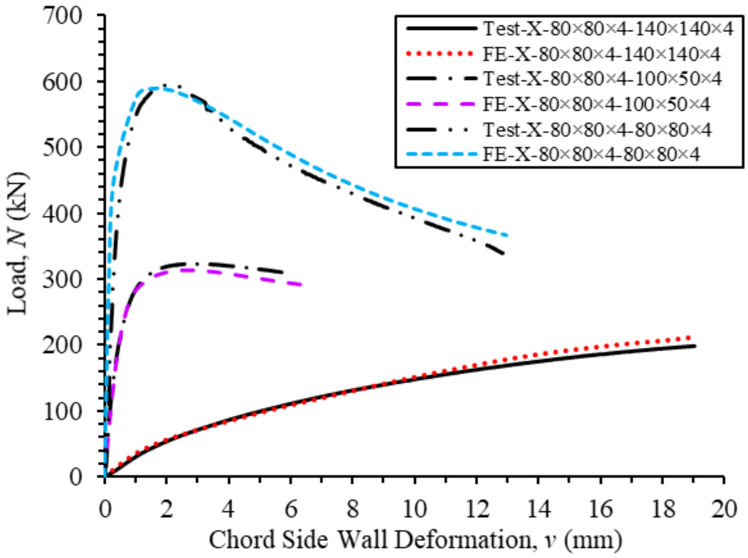

(b) Load vs chord side wall deformation curves.

Fig. 4. Test vs FE load-deformation curves for RHS X-joints at room temperature.

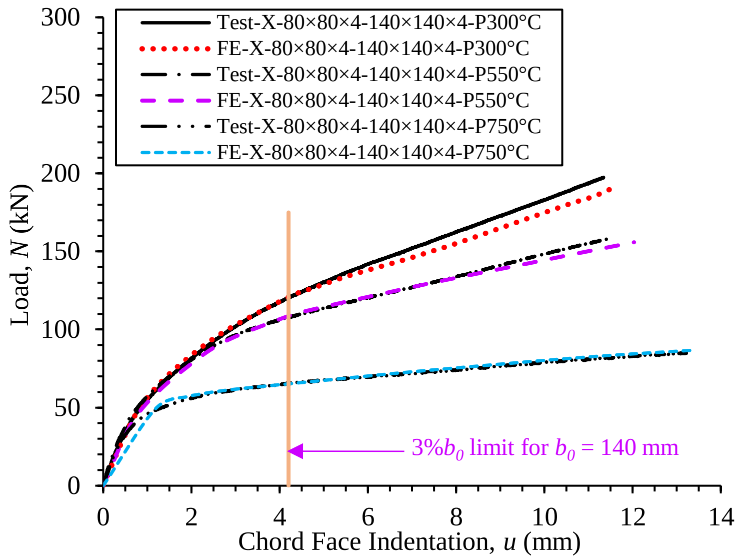

(a) Load vs chord face indentation curves.

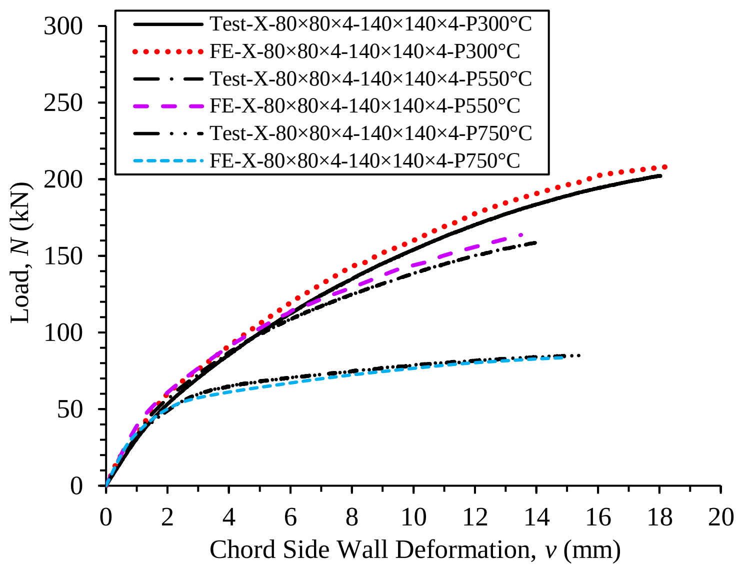

(b) Load vs chord side wall deformation curves.

Fig. 5. Test vs FE load-deformation curves for RHS X-joints for post-fire conditions.

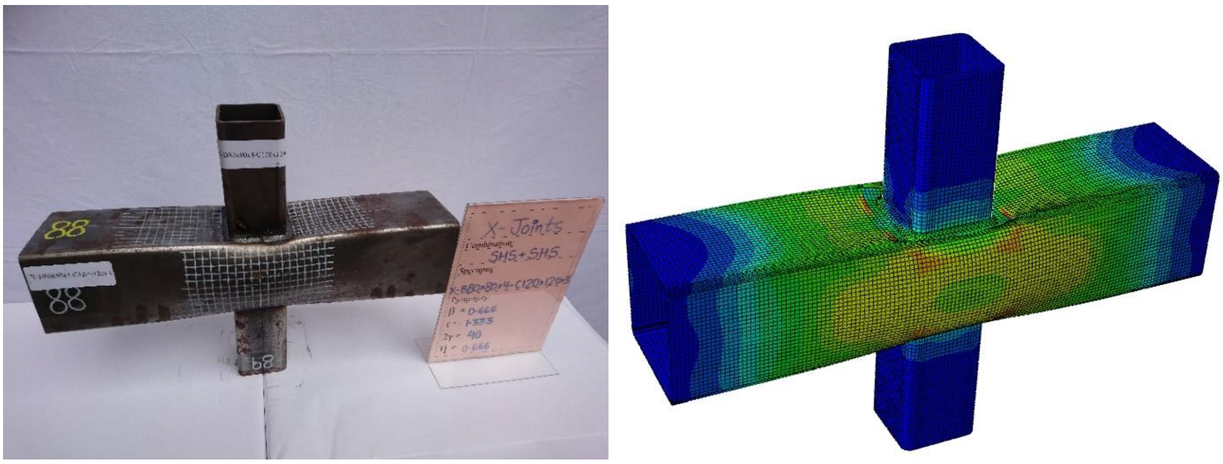

(a) Test vs FE comparison for RHS X-joint failed by F mode at room temperature.

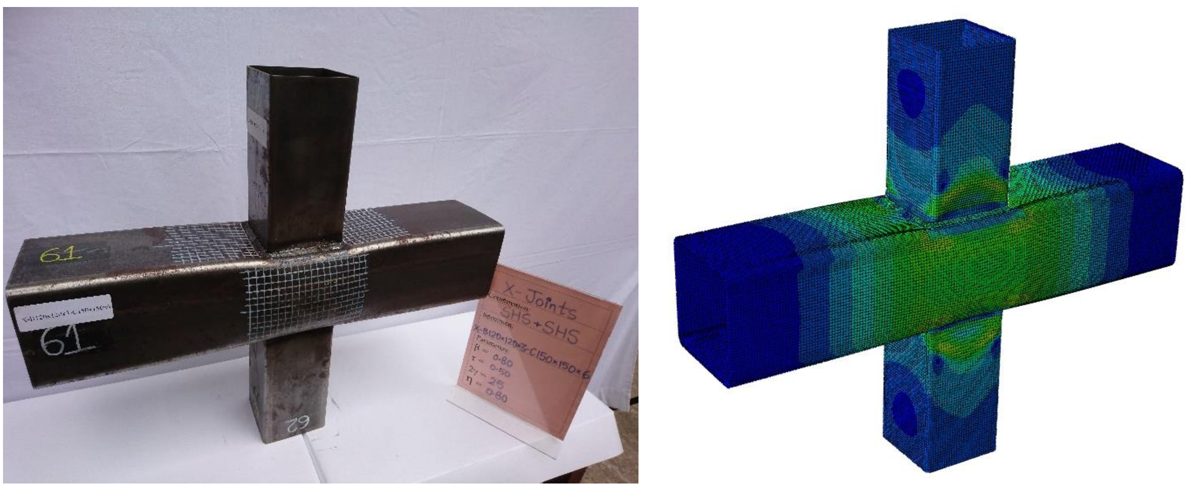

(b) Test vs FE comparison for RHS X-joint failed by F+S mode at room temperature.

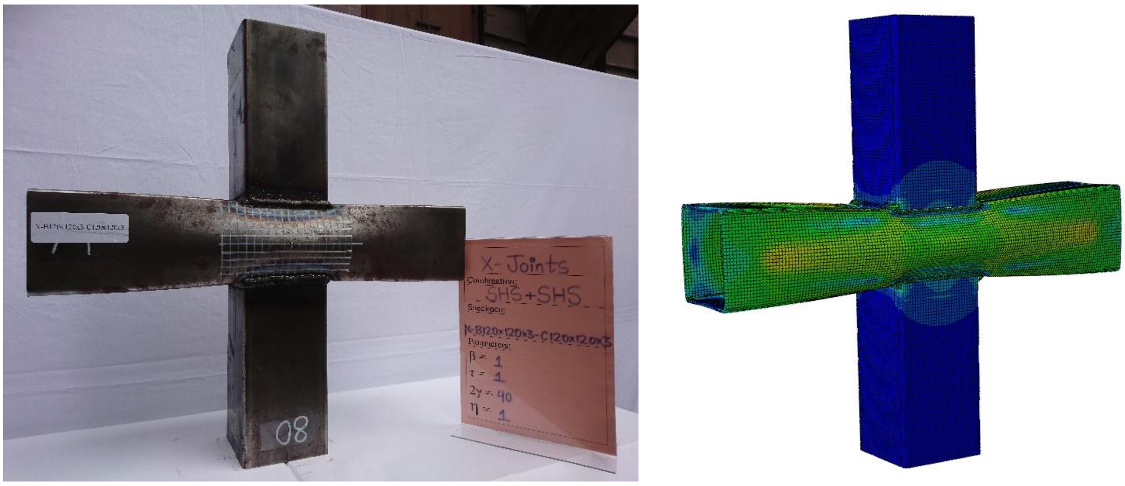

(c) Test vs FE comparison for RHS X-joint failed by S mode at room temperature.

Fig. 6. Test vs FE comparisons of failure modes for RHS X-joints at room temperature.

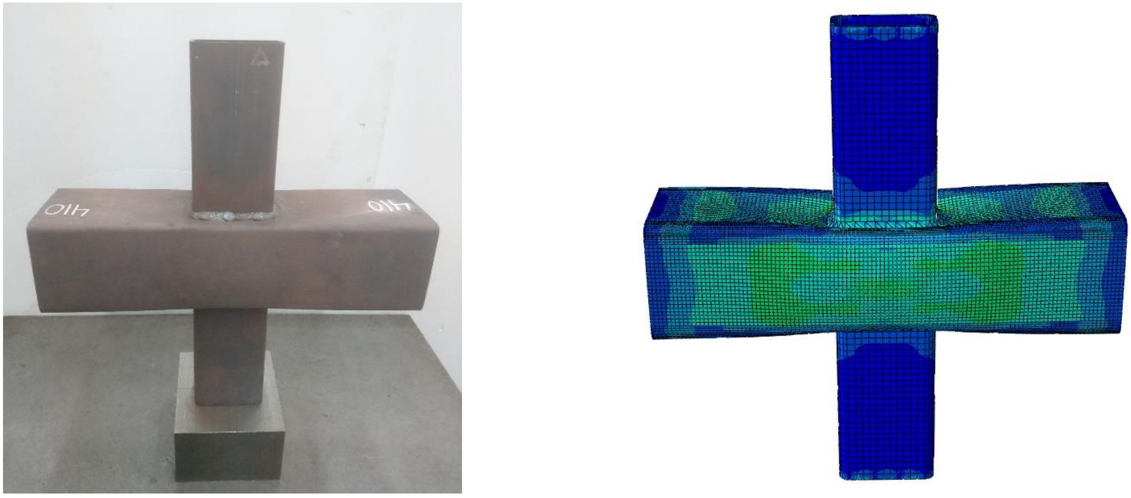

(a) Test vs FE comparison for RHS X-joint failed by F mode for post-fire condition.

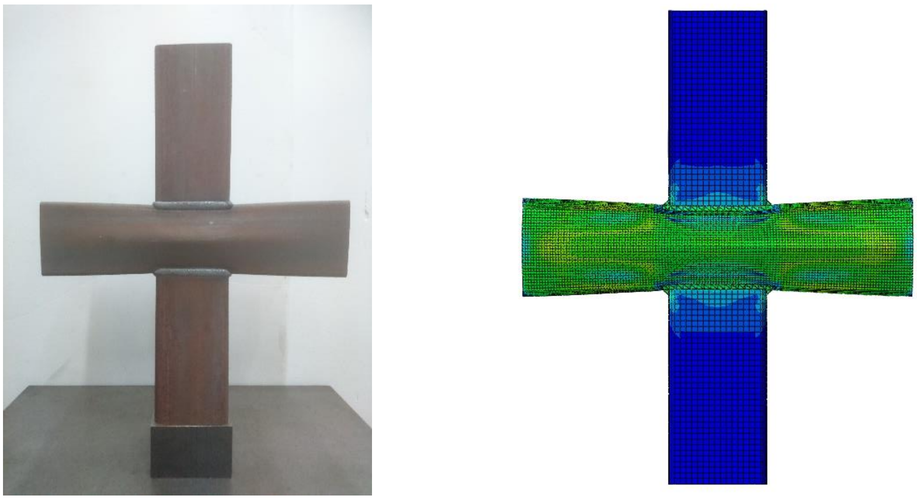

(b) Test vs FE comparison for RHS X-joint failed by S mode for post-fire condition.

Fig. 7. Test vs FE comparisons of failure modes for RHS X-joints for post-fire conditions.

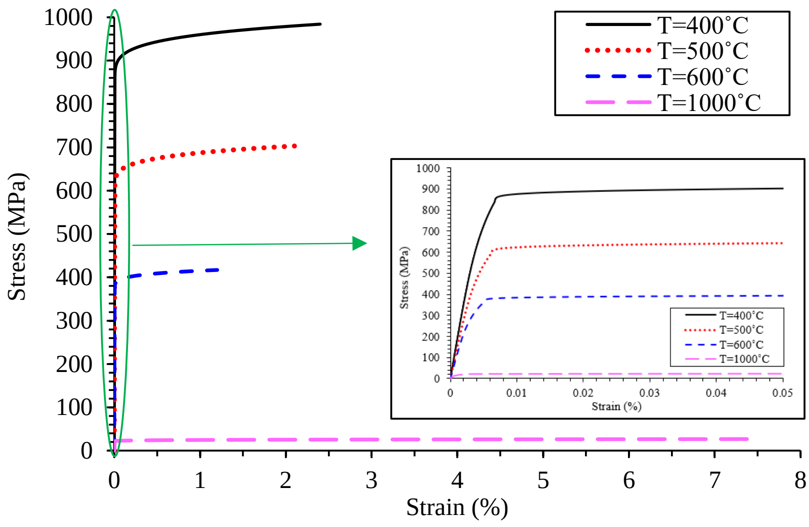

Fig. 8. Elevated temperature stress-strain curves [51].

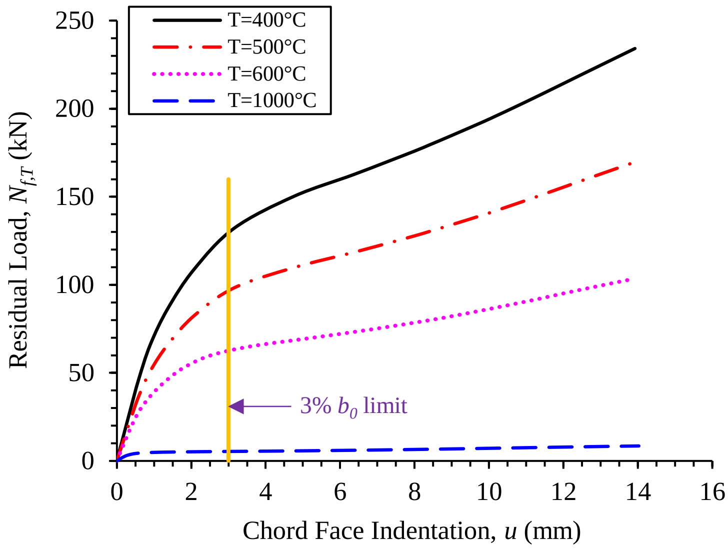

Fig. 9. Variations of load vs deformation curves for typical RHS X-joint (X-30×30×4.5-100×100×6; β=0.30) failed by F mode at elevated temperatures.

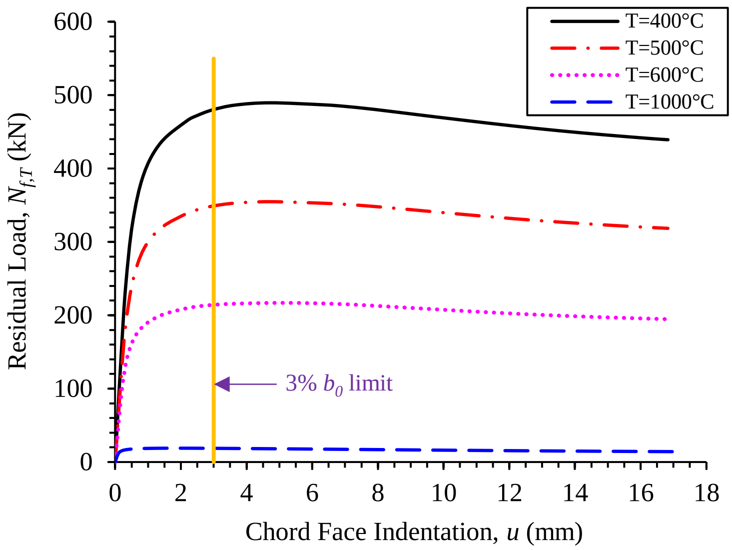

Fig. 10. Variations of load vs deformation curves for typical RHS X-joint (X-80×60×4.5-100×100×6; β=0.80) failed by F+S mode at elevated temperatures.

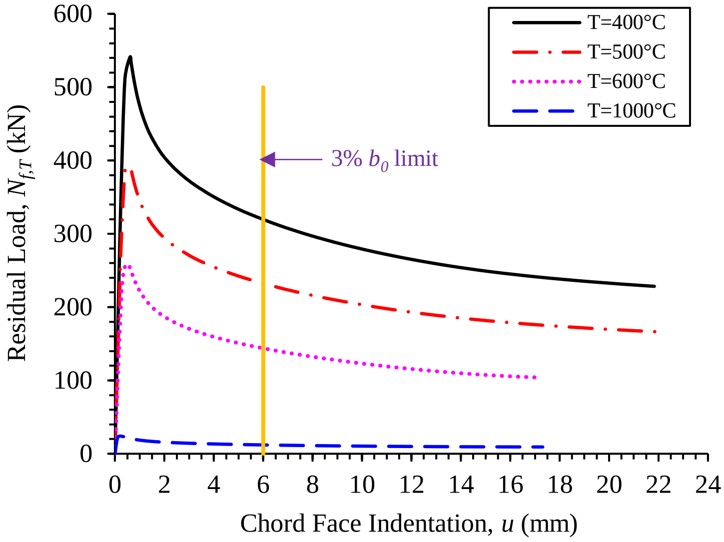

Fig. 11. Variations of load vs deformation curves for typical RHS X-joint (X-200×120×5-200×100×4; β=1.0) failed by S mode at elevated temperatures.

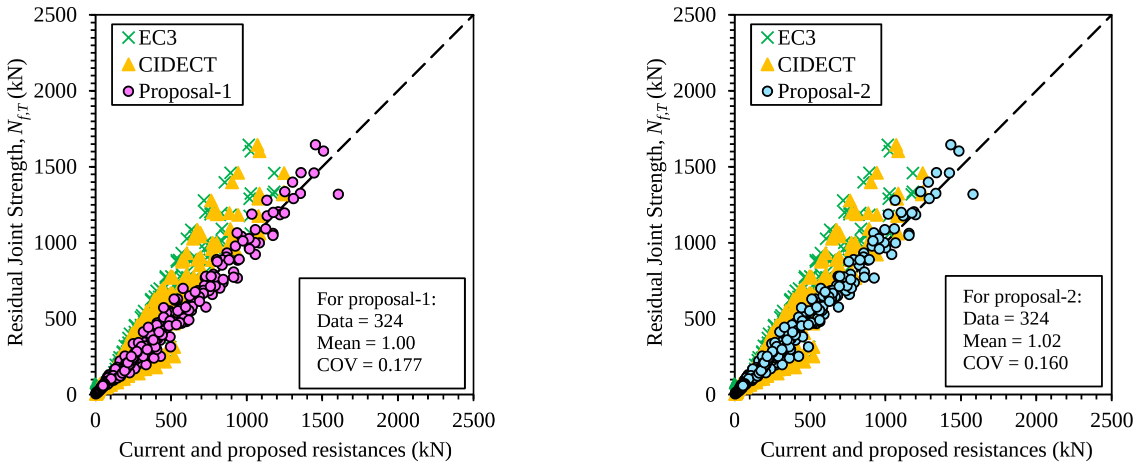

(a) For Proposal-1. (b) For Proposal-2.

Fig. 12. Comparisons of joint resistances at elevated temperatures with current and proposed nominal resistances for RHS X-joints failed by F mode.

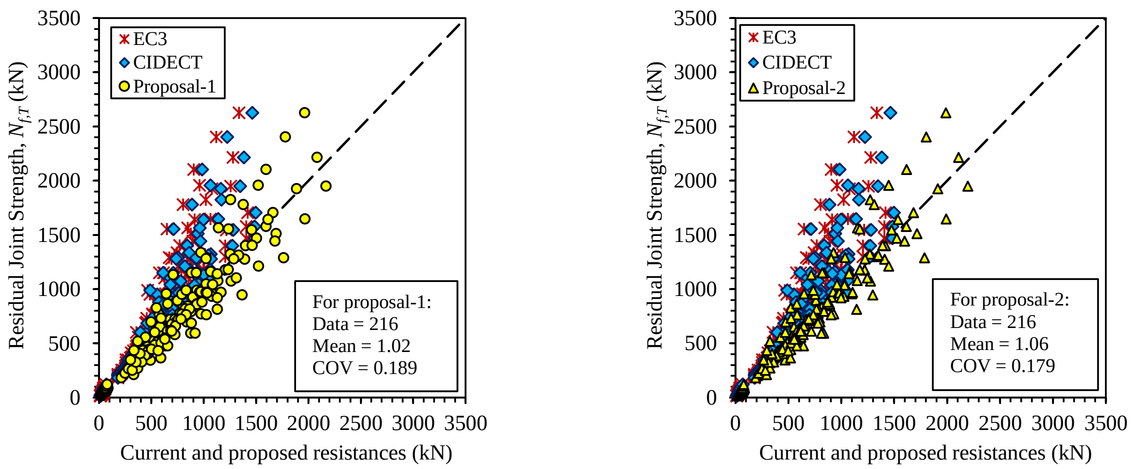

(a) For Proposal-1. (b) For Proposal-2.

Fig. 13. Comparisons of joint resistances at elevated temperatures with current and proposed nominal resistances for RHS X-joints failed by F+S mode.

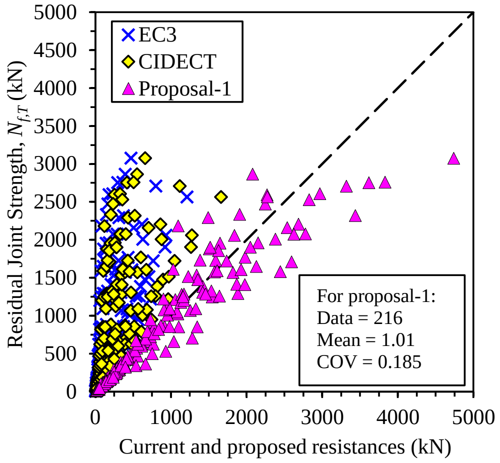

(a) For Proposal-1.

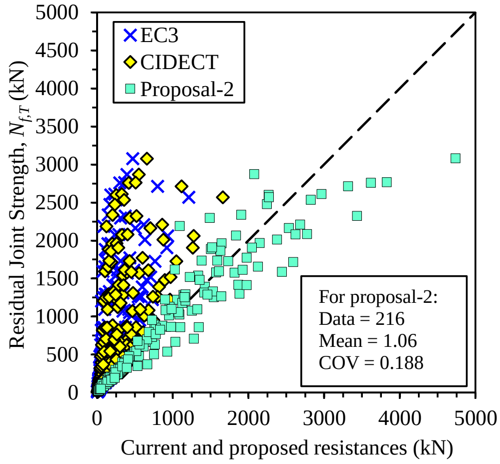

(b) For Proposal-2.

Fig. 14. Comparisons of joint resistances at elevated temperatures with current and proposed nominal resistances for RHS X-joints failed by S mode.

Table 1. Mechanical properties at elevated temperatures [51].

Temperatures (°C)	Nominal Yield Strengths (MPa)	Mechanical properties at elevated temperatures				
		E_0 (GPa)	$\sigma_{0.2}$ (MPa)	σ_u (MPa)	$0.80\sigma_u$ (MPa)	ε_u (%)
21	900	207	1024	1181	945	2.4
400	900	179	839	984	787	2.4
500	900	143	594	703	562	2.1
600	900	114	368	417	334	1.2
1000	900	30	21	27	22	7.4

Table 2. Overall ranges of critical parameters used in parametric study.

Parameters	Validity Ranges
T	[400°C to 1000°C]
β (b_1/b_0)	[0.30 to 1.0]
2γ (b_0/t_0)	[16.6 to 50]
h_0/t_0	[10 to 60]
η (h_1/b_0)	[0.3 to 1.2]
τ (t_1/t_0)	[0.75 to 1.25]

Table 3. Summary of comparisons between joint resistances at elevated temperatures with existing and proposed nominal resistances for RHS X-joints failed by F mode.

Elevated Temperatures (T)	Parameters	Comparisons			
		$\frac{N_{f,T}}{N_{E,T}}$	$\frac{N_{f,T}}{N_{C,T}}$	$\frac{N_{f,T}}{N_{pn1}}$	$\frac{N_{f,T}}{N_{pn2}}$
400°C	No. of data (n)	81	81	81	81
	Mean (P_m)	1.16	1.10	1.01	1.02
	COV (V_p)	0.302	0.302	0.163	0.163
500°C	No. of data (n)	81	81	81	81
	Mean (P_m)	1.22	1.15	0.97	1.03
	COV (V_p)	0.293	0.293	0.157	0.157
600°C	No. of data (n)	81	81	81	81
	Mean (P_m)	1.12	1.11	0.93	1.02
	COV (V_p)	0.251	0.251	0.144	0.144
1000°C	No. of data (n)	81	81	81	81

	Mean (P_m)	1.59	1.59	1.12	1.01
	COV (V_p)	0.203	0.203	0.177	0.177
Overall	No. of data (n)	324	324	324	324
	Mean (P_m)	1.27	1.24	1.00	1.02
	COV (V_p)	0.297	0.306	0.177	0.160
	Resistance factor (ϕ)	1.00	1.00	0.75	0.80
	Reliability index (β_0)	1.83	1.83	2.61	2.53

Table 4. Summary of comparisons between joint resistances at elevated temperatures with existing and proposed nominal resistances for RHS X-joints failed by F+S mode.

Elevated Temperatures (T)	Parameters	Comparisons			
		$\frac{N_{f,T}}{N_{E,T}}$	$\frac{N_{f,T}}{N_{C,T}}$	$\frac{N_{f,T}}{N_{pn1}}$	$\frac{N_{f,T}}{N_{pn2}}$
400°C	No. of data (n)	54	54	54	54
	Mean (P_m)	1.39	1.27	1.05	1.04
	COV (V_p)	0.205	0.196	0.174	0.174
500°C	No. of data (n)	54	54	54	54
	Mean (P_m)	1.42	1.29	0.99	1.04
	COV (V_p)	0.206	0.198	0.176	0.176
600°C	No. of data (n)	54	54	54	54
	Mean (P_m)	1.25	1.20	0.93	1.05
	COV (V_p)	0.202	0.193	0.182	0.182
1000°C	No. of data (n)	54	54	54	54
	Mean (P_m)	1.56	1.49	1.11	1.10
	COV (V_p)	0.140	0.146	0.181	0.181
Overall	No. of data (n)	216	216	216	216
	Mean (P_m)	1.40	1.31	1.02	1.06
	COV (V_p)	0.202	0.199	0.189	0.179
	Resistance factor (ϕ)	1.00	1.00	0.75	0.80
	Reliability index (β_0)	2.51	2.44	2.60	2.56

Table 5. Summary of comparisons between joint resistances at elevated temperatures with existing and proposed nominal resistances for RHS X-joints failed by S mode.

Elevated Temperatures (T)	Parameters	Comparisons $\frac{N_{f,T}}{N_{E,T}}$	$\frac{N_{f,T}}{N_{C,T}}$	$\frac{N_{f,T}}{N_{pn1}}$	$\frac{N_{f,T}}{N_{pn2}}$
400°C	No. of data (n)	54	54	54	54
	Mean (P_m)	6.68	4.78	0.96	1.03
	COV (V_p)	0.706	0.701	0.165	0.164
500°C	No. of data (n)	54	54	54	54
	Mean (P_m)	6.57	4.71	1.03	1.08
	COV (V_p)	0.765	0.760	0.216	0.221
600°C	No. of data (n)	54	54	54	54
	Mean (P_m)	4.87	3.56	0.99	1.14
	COV (V_p)	0.691	0.681	0.193	0.174
1000°C	No. of data (n)	54	54	54	54
	Mean (P_m)	2.50	2.00	1.05	0.98
	COV (V_p)	0.461	0.461	0.151	0.149
Overall	No. of data (n)	216	216	216	216
	Mean (P_m)	5.16	3.76	1.01	1.06
	COV (V_p)	0.816	0.791	0.185	0.188
	Resistance factor (ϕ)	1.00	1.00	0.75	0.80
	Reliability index (β_0)	2.46	2.20	2.58	2.51